ATLAS CONF Note

ATLAS-CONF-2017-011

Photo-nuclear dijet production in ultra-peripheral Pb+Pb collisions

The ATLAS Collaboration

6th February 2017

Ultra-peripheral heavy ion collisions provide a unique opportunity to study the parton distributions in the colliding nuclei via the measurement of photo-nuclear dijet production. An analysis of dijet production in ultra-peripheral $\sqrt{s_{\mathrm{NN}}} = 5.02$ TeV Pb+Pb collisions performed using data collected in 2015 is described. The data set corresponds to a total Pb+Pb integrated luminosity of 0.38 nb^{-1}. The ultra-peripheral collisions are selected using a combination of trigger, zero degree calorimeter, and gap requirements. The jets are reconstructed using a combination of anti-k_t algorithm and an underlying-event subtraction procedure. The results of the measurement include cross-sections for photo-nuclear dijet production as a function of different dijet kinematic variables. The cross-sections, not unfolded for detector response, are compared to results from PYTHIA Monte Carlo simulations re-weighted to match a photon spectrum obtained from the STARLIGHT model.

ATLAS-CONF-2017-011
08 February 2017

1 Introduction

In the last two decades, significant interest has developed on the subject of nuclear parton distribution functions (PDFs) and their modifications relative to the proton PDFs. Some of that interest derives from the observations of non-trivial behavior in the nuclear PDFs [1]. At low values of x the nuclear PDFs exhibit suppression, referred to as "shadowing". At larger x values they exhibit an enhancement referred to as "anti-shadowing" and at still larger x values suppression is again observed, known as the "EMC effect". More recently, interest in nuclear PDFs has been driven by the heavy ion physics programs at RHIC and the LHC. An important tool in characterising the hot, dense matter produced in nucleus-nucleus collisions is the modification of hard-scattering processes through final-state interactions of the outgoing partons with this matter. Theoretical predictions that account for nuclear PDF effects, but not the final-state medium effects, provide a crucial baseline for interpreting the nucleus-nucleus data. In addition, there has been much interest in the physics responsible for shadowing [2, 3] and the possibility that it may be connected to non-linear evolution of the PDFs at high parton density [4, 5, 6].

Unfortunately, information regarding nuclear PDFs, especially their behavior at low x has been limited by lack of experimental data. Most of the data used in global nuclear PDF fits were obtained from fixed target experiments completed more than a decade ago [7, 8]. More recent data from proton- and/or deuteron-nucleus (p+A and/or d+A) collisions at RHIC and the LHC suffer from theoretical uncertainties in translating hadronic hard-scattering processes to constraints on the PDFs.

An alternative method for studying nuclear parton distributions using photo-nuclear production of dijets was proposed a decade ago [9]. The possibility for studying such collisions results from the large flux of virtual photons accompanying large-Z nuclei in ultra-relativistic nucleus-nucleus collisions. Photons with sufficiently long wavelengths couple to the entire nucleus and the cross-sections for photon-induced processes are enhanced by a factor of Z^2. A characteristic transverse momentum (k_{T}) scale for these coherently-emitted photons is $k_{\mathrm{T}} \approx \hbar c/d \approx 15$ MeV, for a Pb nucleus with a diameter, d, of approximately 14 fm. The virtualities of the photons are small compared to the typical scales of a hard-scattering process, making them effectively real. In the longitudinal direction the characteristic momentum scale over which the nuclear enhancement in the photon flux persists is multiplied by an additional Lorentz boost factor. As a result, the enhancement extents to energies ~ 50 GeV which are energetic enough to stimulate hard-scattering processes at low x in the nucleus. For photo-nuclear processes in Pb+Pb collisions, the total enhancement compared to pp collisions is $Z^2A \sim 1.5 \times 10^6$, and the resulting rates for photon-nucleus scattering processes are large enough to be measurable at the LHC. Such collisions are often referred to as "ultra-peripheral" because they can occur when the impact parameters between the incoming nuclei are large such that there is no hadronic interaction between the nuclei.

Photo-nuclear dijet production represents only a subset of ultra-peripheral Pb+Pb collisions that can be studied at the LHC. Indeed, ATLAS has recently produced a preliminary measurement of di-muon production in ultra-peripheral photon-photon collisions [10]. While that process is primarily governed by QED, and thus is not directly relevant to this measurement, it does provide an important experimental constraint on photon fluxes in ultra-peripheral Pb+Pb collisions. Another class of ultra-peripheral collision more directly related to the measurements described here involve exclusive vector meson production [11, 12, 13, 14, 13]. The exclusive nature and the different virtualities probed in such processes makes exclusive vector meson measurements complementary to the measurements presented here, which have a hard scale determined by the jet transverse momenta and/or the jet system mass.

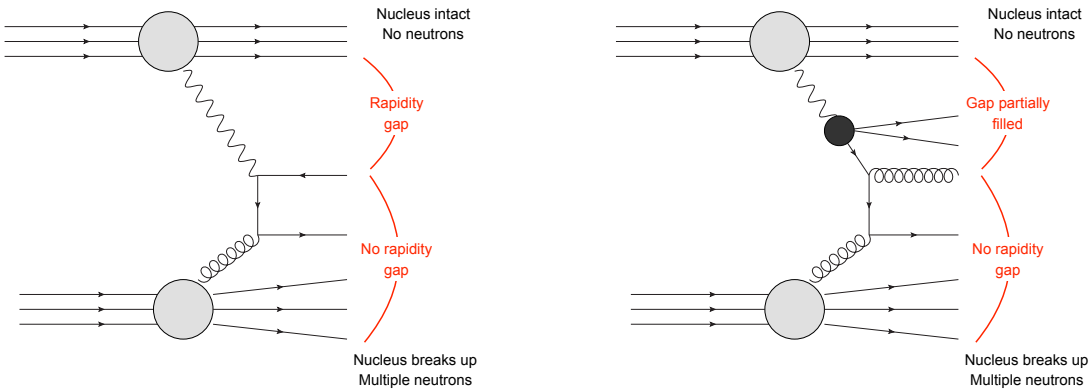

Figure 1: Diagrams representing different types of leading-order contributions to dijet production in high-energy photo-nuclear collisions. The left diagram represents the direct contribution in which the photon itself participates in the hard scattering. The right diagram represents the "resolved" contribution in which virtual excitations of the photon, into a state involving at least a $q\bar{q}$ pair and possibly multiple gluons, participates in the hard scattering in the target nucleus.

The simplest picture of a photo-nuclear reaction is "direct" photo-production. This process, depicted in the left panel of Fig. 1, occurs when the photon acts like a point-like object interacting with the partons in the other nucleus. However, "resolved" processes may also occur in which virtual excitations of the photon may also be probed by the hard interaction in which case the photon serves as a source of partons. In this contribution, depicted in the right panel of Fig. 1, only a fraction of the photon's four-momentum contributes to the hard scattering. Hard photo-production was studied extensively at HERA, where the interplay between the direct and resolved contributions was exploited to study the partonic structure of both the proton and the photon [15, 16].

As neither type of process involves the exchange of color with the photon-emitting nucleus, no significant particle production is expected in the rapidity region between the dijet system and that nucleus. Thus a rapidity gap is expected, and a requirement of a minimum rapidity gap may be used to separate photo-nuclear events from hadronic Pb+Pb collisions. The gap is expected to be smaller in resolved photon events due to the additional particle production associated with the "photon-remnant". This was also studied at HERA [17], and these measurements provide important experimental input into the modeling of resolved photon processes by event generators.

The photon-emitting nucleus is also expected to produce few or no neutrons because the photon flux is largest for momenta in the range where they couple to the entire nucleus. The emission of such photons is not expected to excite the nucleus. Thus a combination of a rapidity gap and zero neutrons in the same direction provide straightforward criteria to identify these events experimentally. However, additional soft photon exchanges during the ultra-peripheral collision can cause the photon-emitting nucleus to be excited into low-lying states where it may emit a small number of evaporation neutrons and a measurement must either correct for this effect or be compared to a theoretical model that includes it.

This note presents a measurement of photo-nuclear jet production cross-sections in Pb+Pb collisions at a per nucleon center-of-mass energy of $\sqrt{s_{\mathrm{NN}}} = 5.02$ TeV, recorded in 2015. Photo-nuclear events are identified by requirements on the number of neutrons in the acceptance of the ATLAS zero degree calorimeters and the presence of rapidity gaps in the main detector. Specifically, events are required to

have zero neutrons in one direction and one or more neutrons in the opposite direction, referred to as the "0nXn" event topology. The photon-going direction is defined to be the direction in which zero neutrons are observed. Background events are removed by requiring a minimum rapidity gap in this direction and requiring that there is no large gap in the opposite direction. Corrections are applied to account for signal events removed by these requirements, and thus they are not part of the fiducial definition of the measurement. Event-level observables are constructed from all jets having transverse momenta $p_{\mathrm{T}} > 15$ GeV and pseudo-rapidities $|\eta| < 4.4$. Events are required to have two or more such jets and at least one jet with $p_{\mathrm{T}} > 20$ GeV. The jets are used to define the event-level variables:

$$H_{\mathrm{T}} \equiv \sum_i p_{\mathrm{T}\,i}\,, \quad m_{\mathrm{jets}} \equiv \left[\left(\sum_i E_i\right)^2 - \left|\sum_i \vec{p}_i\right|^2\right]^{1/2}, \quad y_{\mathrm{jets}} \equiv \frac{1}{2}\ln\left(\frac{\sum_i E_i + \sum_i p_{z\,i}}{\sum_i E_i - \sum_i p_{z\,i}}\right), \tag{1}$$

where i runs over the measured jets in an event, E and $\vec{p}$ represent jet energies and momentum vectors, respectively, and p_z represents the longitudinal component of the jet momenta. The signs of p_z are chosen to be positive in the photon-going direction. A further requirement is imposed that the jet-system mass, m_{jets}, satisfies $m_{\mathrm{jets}} > 35$ GeV.

The differential cross-sections are measured as a function of H_{T} and

$$z_\gamma \equiv \frac{m_{\mathrm{jets}}}{\sqrt{s}} e^{+y_{\mathrm{jets}}}\,, \quad x_{\mathrm{A}} \equiv \frac{m_{\mathrm{jets}}}{\sqrt{s}} e^{-y_{\mathrm{jets}}}\,. \tag{2}$$

In the limit of $2 \to 2$ scattering kinematics, x_{A} corresponds to the ratio of the energy of the struck parton in the nucleus to the (per nucleon) beam energy. $z_\gamma = x_\gamma y$, where y is the energy fraction carried by the photon. For direct processes, x_γ is unity, while for resolved events, it is the fraction of the photon's energy carried by the resolved parton entering the hard scattering.

The remainder of this note is structured as follows: Section 2 describes the ATLAS detector and the triggers used for the measurements in this analysis. Section 3 describes the data and Monte Carlo (MC) samples used in the analysis and provides information on how the MC sample obtained from Pythia is re-weighted for use in Pb+Pb collisions. Section 5 describes all aspects of the data analysis and the measurement of the photo-nuclear dijet production cross-sections. Section 6 discusses the evaluation of the systematic uncertainties, and Section 7 discusses possible backgrounds to the measurement. Section 8 presents the final results figures with comparison to Monte Carlo and theory. Section 9 summarizes this note and provides conclusions.

2 ATLAS detector

The measurements described in this note are performed using the ATLAS detector [18] in the Run 2 configuration. They rely on the calorimeter system, the inner detector, the zero degree calorimeters, and the trigger system. The calorimeters, which cover the pseudo-rapidity range $|\eta| < 4.9$[1], are used for measuring the jets and for the rapidity gap analysis. The inner detector is used to measure charged particle tracks over $|\eta| < 2.5$. The zero degree calorimeters (ZDCs), which measure neutrons emitted at

[1] ATLAS uses a right-handed coordinate system with its origin at the nominal interaction point (IP) in the center of the detector and the z-axis along the beam pipe. The x-axis points from the IP to the center of the LHC ring, and the y-axis points upward. Cylindrical coordinates (r, ϕ) are used in the transverse plane, ϕ being the azimuthal angle around the z-axis. The pseudorapidity is defined in terms of the polar angle θ as $\eta = -\ln\tan(\theta/2)$.

small rapidity separation from the incident nuclei, were used for triggering and for offline event selection. The ZDCs are located a distance of ±140 m from the nominal interaction point and cover $|\eta| > 8.3$. Each calorimeter consists of four modules, and each module contains one interaction length of tungsten absorber.

The ATLAS trigger system consists of a Level-1 trigger followed by a processor-based high-level trigger (HLT) that can apply algorithms similar to those used in offline analysis. Level-1 ZDC triggers were obtained, separately, from each calorimeter. These required the total energy in the given ZDC to be above a threshold set well below the single-neutron energy. The primary triggers used for this measurement required detection of at least one neutron in only one of the ZDCs, a minimum total transverse energy, $\sum E_{\mathrm{T}}$, measured in the calorimeters of 5 GeV, and a maximum $\sum E_{\mathrm{T}}$ of 200 GeV, all applied at Level-1. One trigger required only these conditions (UPC) while two additional triggers combined this Level-1 trigger with HLT selections on "central" ($|\eta| < 3.2$) jets (UPC-Jet) or "forward" ($|\eta| > 3.2$) jets (UPC-FWJet). The HLT jet reconstruction used the ATLAS heavy ion jet reconstruction and background subtraction procedure applied to anti-k_t $R = 0.4$ jets.

3 Data sets and reconstruction

3.1 Pb+Pb data

In 2015, ATLAS recorded a Pb+Pb data set corresponding to a total luminosity of $0.48\,\mathrm{nb}^{-1}$. The luminosity was calibrated using established methods [19] from measurements performed during three beam-separation (van der Meer) scans carried out during the 2015 Pb+Pb run. The combined systematic uncertainty on the luminosity calibration and luminosity measurements for the current (preliminary) calibration is 6.1%

The triggers used for this measurement sampled a fraction of the total luminosity; the UPC trigger sampled an integrated luminosity of $95\,\mu\mathrm{b}^{-1}$, while the UPC-Jet and UPC-FWJet triggers sampled luminosities of $300\,\mu\mathrm{b}^{-1}$ and $380\,\mu\mathrm{b}^{-1}$, respectively. A total of 100047, 116090, and 5740 events were recorded for the UPC, UPC-Jet, and UPC-FWJet triggers, respectively.

3.2 Monte Carlo samples

The primary Monte Carlo sample for this analysis was obtained from Pythia version 6.41 [20] using the Perugia2012 tune [21] configured for $\gamma^* + p$ collisions with the photons produced via bremsstrahlung from a muon beam (`gamma/mu+` mode). The muon-proton center of mass energy was 5.02 TeV. The Pythia generator was configured to include the default combination of three photo-production processes: direct, vector meson dominance (VMD), and anomalous. The VMD mechanism treats the photon as a vector meson and describes the hard-scattering process as a meson-proton interaction. The anomalous contribution interpolates between the lower-Q^2 virtual excitations of the photon described by the VMD mechanism and the harder virtual excitations for which it samples the photon parton distribution. The VMD and anomalous mechanisms together describe the resolved-photon contribution to dijet photo-production. The Pythia event generation used the CTEQ6L1 proton PDF set and the SaS 1D photon PDFs [22, 23] for the anomalous processes. To match the kinematics of the UPC photo-nuclear events in the measurement, the photon virtuality was limited to $\sqrt{Q^2} \lesssim 30$ MeV and the minimum photon-proton invariant mass

was set to 15 GeV. The photo-nuclear dijets were sampled over a wide kinematic range by filtering the Pythia-generated events according to the leading jet p_{T} using three sample ranges: $7 < p_{\mathrm{T\,lead}} < 20$ GeV, $20 < p_{\mathrm{T\,lead}} < 60$ GeV, and $60 < p_{\mathrm{T\,lead}} < 160$ GeV. Here, and for the remainder of this note, "leading" refers to the jet having the highest transverse momentum in the event, while "sub-leading" refers to the jet having the second-highest transverse momentum. For each of the $p_{\mathrm{T\,lead}}$ intervals, 500,000 events were produced for each of the two possible photon directions.

A separate sample of 100,000 Herwig++ [24] 5.02 TeV pp events were generated with exclusive production of $q\bar{q}$ pairs via the process $\gamma + \gamma \rightarrow q\bar{q}$. The events were sampled according to the StarLight [25] photon spectrum and are used to evaluate potential backgrounds to this measurement.

The Pythia- and Herwig++-generated events were passed through a GEANT4 [26] simulation of the ATLAS detector response [27] and analyzed in the same manner as ATLAS data.

4 Theory and models

To compare to the measured cross-sections presented in this note, a model was constructed combining elements of Pythia and the StarLight [25] generator. This model, referred to as Pythia+StarLight in the rest of this note, is described in the following.

The cross-section for photo-nuclear dijet production can be calculated using the formalism of the equivalent photon-approximation (EPA). Pythia is capable of simulating photon-nucleon events using the equivalent photon flux from a lepton beam as the source of photons, providing a mixture of direct and resolved processes described in the previous section. Despite the sophisticated description of photon-nucleon interactions contained in Pythia, it is insufficient to satisfactorily describe photo-nuclear dijet production. Specifically, the photon spectrum it uses is not appropriate for nuclear collisions. Furthermore, in nucleus-nucleus collisions, when the impact parameter approaches twice the nuclear radius, hadronic interactions become prevalent and greatly alter the characteristics of the events. Such interactions will result in particle production over the entire rapidity range and will cause the photon-emitting nucleus to break up. These features result in events that are nearly identical to those where a photo-nuclear reaction did not occur making an experimental identification of the photo-nuclear processes impossible. These effects can be accounted for by applying a reweighting to Pythia to provide a flux integrated over impact parameter that contains these effects.

StarLight [25] is a Monte Carlo model and event generator that has been used to simulate two-photon and photon-pomeron scattering in heavy ion collisions. The model has been tested using data from both RHIC and the LHC including a preliminary ATLAS measurement of $\gamma + \gamma \rightarrow \mu^+\mu^-$ production in 5.02 TeV Pb+Pb collisions [10]. In that measurement, StarLight was found to reproduce well the shape and absolute normalization of the measured di-muon spectrum. StarLight uses the equivalent photon approximation to calculate these cross-sections and for nucleus-nucleus collisions, the formalism uses classical electrodynamics to calculate the energy flux from the charge distribution of the nucleus and then reinterprets this energy flux as $E\,N_\gamma^{\mathrm{A}}$, where E represents the photon energy and N_γ^{A} the number of photons associated with the nucleus. For a point charge,

$$\frac{\mathrm{d}N_\gamma^{\mathrm{A}}}{\mathrm{d}E\mathrm{d}^2b} = \alpha_{\mathrm{EM}}\frac{Z^2}{\pi^2\gamma_{\mathrm{L}}^2}\frac{E}{(\hbar c)^2}\left(K_1^2(\xi) + \frac{1}{\gamma_{\mathrm{L}}^2}K_0^2(\xi)\right), \quad \xi = \frac{Eb}{\hbar c}\frac{1}{\gamma_{\mathrm{L}}}, \tag{3}$$

where $\gamma_L = E_A/m_A$ is the (longitudinal) Lorentz boost factor and K_n are modified Bessel functions of order n. The quantities, E_A and m_A, represent the total energy and total mass of the nucleus, respectively. At high energies, the γ_L is so large that the second term can be neglected, as is the case in STARLIGHT.

As discussed above, the experimentally accessible part of the photo-nuclear cross-section only receives contributions from events where there are no additional hadronic interactions. Thus the cross-section must be multiplied by a factor $P_{UPC}(b)$, where b is the impact parameter of the collision. STARLIGHT also contains a model of the nuclear geometry and hadronic interactions and can be used to calculate $P_{UPC}(b)$.

For the process $A + B \to \gamma + B \to X$, the EPA cross-section is:

$$\frac{d\sigma^{AB}_{EPA}}{d^2r_A d^2r_B dE} \equiv \frac{dN^A_\gamma}{dE d^2r_A}\frac{d\sigma^{\gamma B}}{d^2r_B}, \tag{4}$$

where r_A and r_B denote coordinates in the transverse plane of the target and projectile nuclei A and B, respectively. The cross-section for $\gamma + B$ scattering can be expressed in terms of the $\gamma + N$ cross-section and the nuclear thickness function $T_B(r_b)$, which is the transverse density of nucleons in the nucleus per unit area,

$$\frac{d\sigma^{\gamma B}}{d^2r_B} = T_B(r_b)\sigma^{\gamma N}. \tag{5}$$

The total cross-section is obtained by multiplying by P_{UPC} and integrating over the projectile and target. Thus,

$$\frac{d\sigma^{Pb+Pb}_{UPC}}{dE} = 2\int d^2b\, P_{UPC}(b)\int d^2r_B \left.\frac{d^2N^{Pb}_\gamma}{dE\, d^2r_A}\right|_{\vec{r_A}=\vec{b}-\vec{r_B}} T_{Pb}(r_B)\sigma^{\gamma N} \equiv \frac{dN^{eff}_\gamma}{dE}\sigma^{\gamma N}, \tag{6}$$

where factor of 2 has been inserted to account for the symmetry of the Pb+Pb collision system. The PYTHIA + STARLIGHT model is constructed by using STARLIGHT to obtain dN^{eff}_γ/dE and evaluating a weight,

$$w(E) \equiv \frac{dN^{eff}_\gamma}{dE} \Big/ \frac{dN^{PYTHIA}_\gamma}{dE}, \tag{7}$$

which is applied to the generated PYTHIA events. The spectrum, dN^{PYTHIA}_γ/dE, is obtained from the PYTHIA EPA formula [20] evaluated at fixed virtuality $Q^2 = (15\,\text{MeV})^2$.

5 Data analysis

5.1 Reconstruction

The events used for this analysis were reconstructed using a configuration of the ATLAS software typically used in *pp* collisions. The reconstruction of charged particle tracks used the same settings and selections as those applied in minimum-bias measurements [28]. Calorimeter clusters were reconstructed using the same method applied in other ATLAS analyses [29] but with thresholds set appropriately for low-luminosity conditions. The jets were reconstructed using a combination of the anti-k_t [30] algorithm with $R = 0.4$ and the heavy ion subtraction procedure [31] configured for small underlying event energy densities.

Following well-established procedures within ATLAS [32], the jet energies are calibrated initially using constants obtained from MC evaluations of the jet response in $\sqrt{s} = 5$ TeV pp collisions. A set of corrections is applied to the jet energies to account for changes in the jet energy scale (JES) arising from differences in flavor composition between the jets produced in photo-nuclear events and in inclusive jet production in pp collisions. Data-driven corrections are performed to account for differences between data and MC simulations. A relative energy scale calibration (inter-calibration) is performed by evaluating data-MC agreement in the dijet balance between jets in different η regions. The *in situ* calibration uses Z-jet and γ-jet balance to perform an absolute energy scale calibration.

The minimum transverse momenta for charged particles, clusters, and jets used in this analysis are 0.3 GeV, 0.2 GeV, and 15 GeV, respectively. Jets are required to be completely contained within the detector: $|\eta_{\text{jet}}| < 4.4$.

5.2 ZDC calibration and trigger efficiency

The energy measurements in the ZDCs were calibrated using the single-neutron peak which is well-separated from the two-neutron peak in Pb+Pb collisions. In addition to setting the absolute energy scale in the ZDCs the calibration accounts for an instantaneous luminosity- and time-dependent response. The former results from large current draw in the ZDC photo-multiplier tubes at higher luminosities, while the latter results from radiation damage in detector.

For a given event, the photon- and Pb-going directions are evaluated using the ZDC trigger: the side on which the trigger fired (did not fire) is assumed to be the Pb-going (photon-going) direction. Then, the 0nXn topologies are selected by requiring $E_A^{\text{ZDC}} > 1$ TeV and $E_\gamma^{\text{ZDC}} < 1$ TeV, where E_A^{ZDC} and E_γ^{ZDC} are the ZDC energies in the nucleus-going and photon-going directions, respectively. The distribution of calibrated energies divided by the per-nucleon beam energy, $E^{\text{ZDC}}/2.51$ TeV, on the side that fired the ZDC trigger and on the side that did not fire the ZDC trigger are shown in Figure 2. The logarithmic horizontal scale shows the full distribution while also making visible the single-neutron region, but it excludes a large peak at zero for events which did not fire the trigger. The peak in E_γ^{ZDC} near $E_\gamma^{\text{ZDC}}/2.51\,\text{TeV} \sim 1$ results from inefficiency in the level-1 ZDC trigger that allows some 1nXn events to satisfy the 0nXn condition.

At higher luminosities, an inefficiency in the ZDC trigger is observed that primarily results from large energy deposits in preceding collisions. This inefficiency is responsible for the non-zero energies observed in Figure 2 in the photon-going direction. Significant inefficiencies are only observed below and in the vicinity of the single-neutron peak. The trigger inefficiency was measured as a function of E^{ZDC} using Pb+Pb events satisfying a ZDC trigger on the opposite side.

5.3 Gap measurement

The triggers used in this measurement select both UPC events and a class of rapidity-asymmetric hadronic collisions that have characteristics similar to proton-nucleus collisions. These events can be efficiently removed by requiring the presence of a gap in the photon-going direction. The rapidity gap analysis proceeds by applying the same selections on calorimeter clusters as applied in other ATLAS measurements [33]. The resulting clusters and the charged particle tracks are ordered in η and intervals between adjacent tracks or clusters with separation $\Delta\eta > 0.5$ are recorded. The minimum $\Delta\eta$ requirement, excludes small

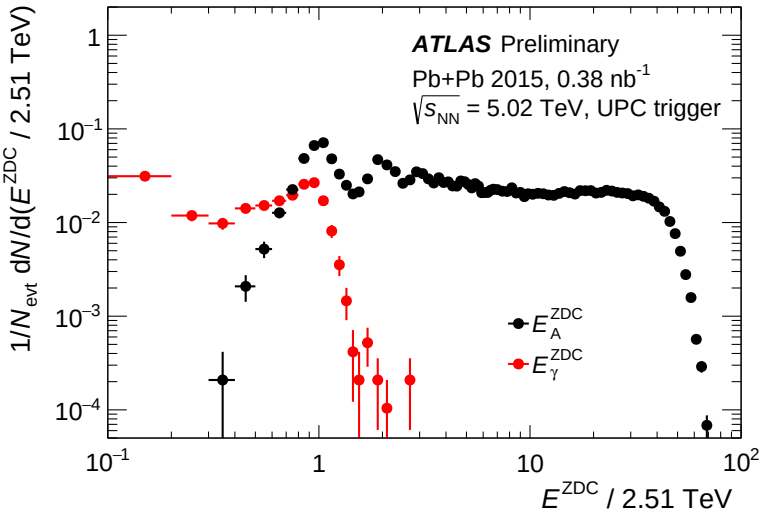

Figure 2: Distributions of ZDC energy in the photon-going and nucleus-going direction for events satisfying the UPC trigger. The vertical line indicates the location of the single-neutron selection applied in the analysis.

gaps that may occur purely due to fluctuations in the particle rapidity density. Any such intervals at the edge of the detector, $\Delta\eta_{\text{edge}}$, are taken as "edge gaps".

Due to the presence of resolved-photon events that can contribute additional particles in the photon-going direction, this analysis primarily relies on the sum of the gaps having $\Delta\eta > 0.5$ that lie between the largest-η and smallest-η jets and the closest detector boundary. The sums on the photon-going and Pb-going sides of the detector will be referred to as $\sum_\gamma \Delta\eta$, and $\sum_A \Delta\eta$, respectively.

Figure 3 demonstrates the results of the gap analysis for events selected by the UPC trigger having at least two jets passing the minimum p_{T} requirement. The left panel shows the correlation between the photo-going edge gap, $\Delta\eta_\gamma^{\text{edge}}$, and $\sum_\gamma \Delta\eta$, while the right panel shows the correlation between $\sum_\gamma \Delta\eta$ and $\sum_A \Delta\eta$. The presence of resolved-photon events can be seen in the left panel as events for which $\sum_\gamma \Delta\eta > \Delta\eta_\gamma^{\text{edge}}$. The right panel shows that there are events having small $\sum_\gamma \Delta\eta$ but large $\sum_A \Delta\eta$. The $\sum_A \Delta\eta < 3$ requirement suppresses the contribution of such events in the region $\sum_\gamma \Delta\eta > 2$.

As suggested above, events selected by the UPC trigger and having two jets look very different depending on whether they have gaps in the photon-going direction or not. This is demonstrated in Figure 4 which shows in the left panel the correlation between charged particle multiplicity, N_{trk}, and $\sum_\gamma \Delta\eta$. Events with small or no gaps, $\sum_\gamma \Delta\eta < 1$, have a much broader multiplicity distribution than the events with larger $\sum_\gamma \Delta\eta$. The right panel in the figure shows the multiplicity distributions for two selections on $\sum_\gamma \Delta\eta$: $\sum_\gamma \Delta\eta < 1$ and $\sum_\gamma \Delta\eta > 2$. The multiplicity distributions are completely different, demonstrating that the events in the two classes arise from different physics.

5.4 Event selection

Events used in the measurement are required to satisfy the 0nXn condition in the ZDCs and to have $\sum_\gamma \Delta\eta > 2$ and $\sum_A \Delta\eta < 3$. The last requirement reduces background from $\gamma + \gamma$ collisions and non-photo-nuclear UPC processes. Events are required to have a reconstructed vertex and at least one charged

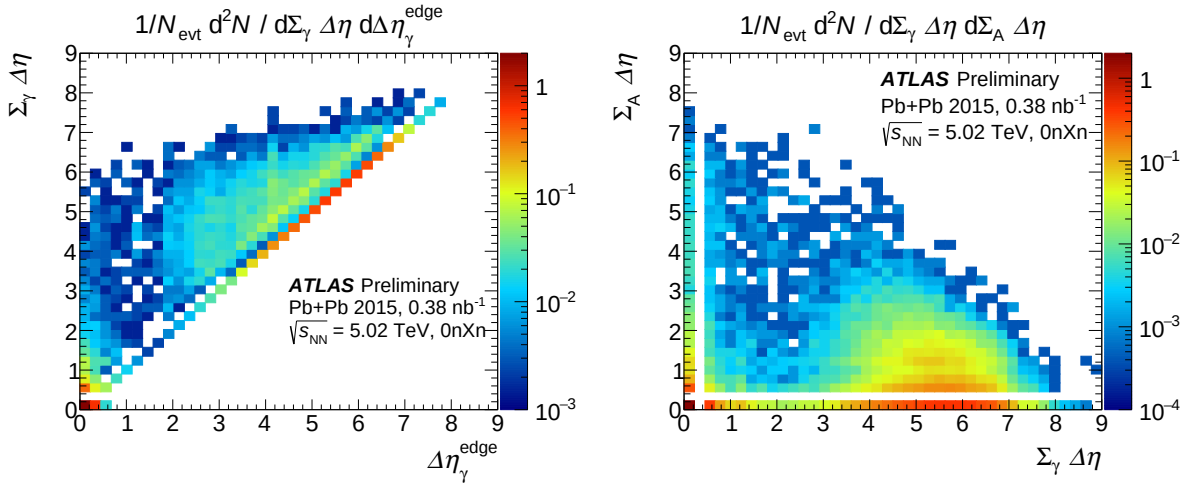

Figure 3: Left: two-dimensional distribution of $\sum_\gamma \Delta\eta$ vs $\Delta\eta_\gamma^{\text{edge}}$ for events selected by the UPC trigger having at least two jets. Right: two-dimensional distribution of $\sum_A \Delta\eta$ versus $\sum_\gamma \Delta\eta$.

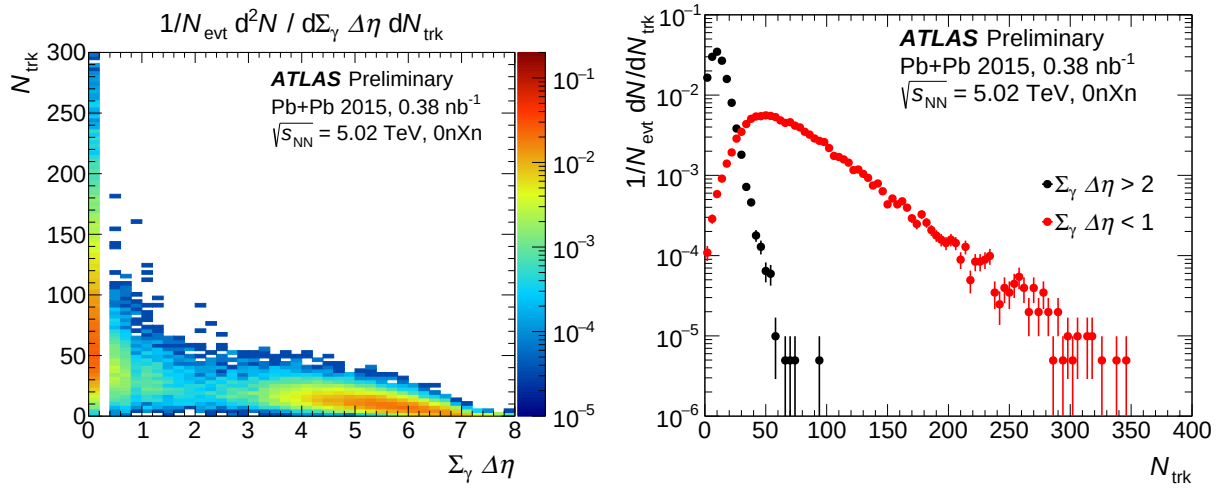

Figure 4: Left: two-dimensional distribution of N_{trk} vs $\sum_\gamma \Delta\eta$ for events selected by the UPC trigger having at least two jets. Right: distributions of charged particle multiplicity for events with $\sum_\gamma \Delta\eta > 2$ and $\sum_\gamma \Delta\eta < 1$.

particle track passing applied selections if at least one of the jets falls within the inner detector acceptance. Events used in the analysis were required to have at least two jets satisfying the $p_{\text{T}}^{\text{jet}} > 15$ GeV and $|\eta| < 4.4$ requirements. Furthermore, the leading jet is required to satisfy $p_{\text{T}_{\text{lead}}} > 20$ GeV. The azimuthal angle difference between the leading and sub-leading jets is required to be greater than 0.2 and the combined mass of all reconstructed jets, m_{jets}, is required to be greater than 35 GeV.

Figure 5 provides a summary of the jet kinematics in events passing the above-described selections. The left panel on the top shows the p_{T} distributions for leading, sub-leading and other jets in the event. The spectra are similar to those observed in other hard-scattering processes though the leading and sub-leading jet spectra at low p_{T} are affected by the p_{T} thresholds applied in the analysis. The panel on the right of the figure shows the leading-sub-leading jet $\Delta\phi$ distribution for events having two, three, or and more than three jets. The dijet events have a $\Delta\phi$ distribution that is sharply peaked at $\Delta\phi = \pi$ while the other

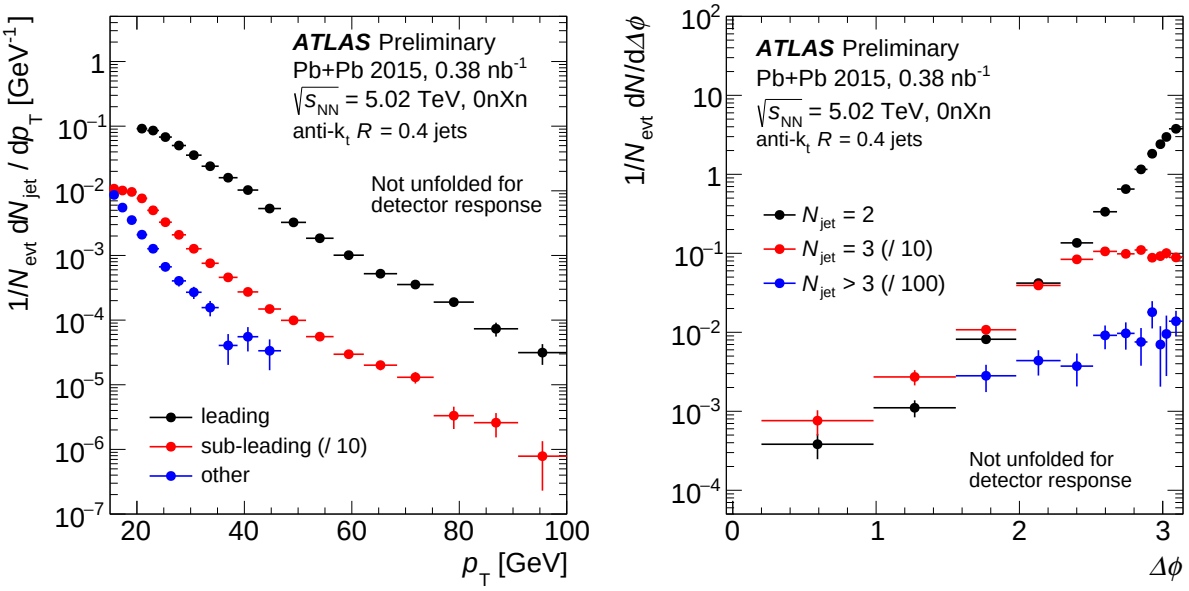

Figure 5: Left: distribution of leading jet, sub-leading jet, and other jet transverse momentum for events included in this analysis. Right: distribution of $\Delta\phi$ between leading and sub-leading jets for events with 2, 3, or more jets.

distributions are much broader confirming that the the additional jets reflects real changes in the topology of the events.

The kinematics of the photo-nuclear hard scattering processes are evaluated as follows. The total four-momentum of the jet system is evaluated by summing the four-vectors for all jets. The rapidity and mass of the jet system, y_{jets} and m_{jets} then determine the kinematics of the photon and the parton from which it scattered according to Eq. 2. The H_{T} variable is computed by summing the transverse momenta of the jets.

5.5 Data-Monte Carlo comparisons

The distributions of various event or jet quantities are compared to the same distributions from the MC sample in Figs. 6–9. Unless stated otherwise, the events used to produce the distributions satisfy all of the above-described event selection criteria on reconstructed quantities for both the data and the MC. Each figure compares distributions in the data to those from un-reweighted (Pythia) and reweighted (Pythia+STARlight) MC to demonstrate the sensitivity of the observable to the shape of the true z_γ distribution and to demonstrate the level of agreement between the data and MC.

Figure 6 shows the actual z_γ distributions. Prior to reweighting, the z_γ spectrum produced by Pythia is much harder than that observed in the measurement. After reweighting, the distributions agree well over most of the z_γ range, though an z_γ-dependent difference is observed at the smallest z_γ values.

Figure 7 compares $\sum_\gamma \Delta\eta$ distributions between data and MC. Similar to the behavior observed for the z_γ distributions, the un-reweighted MC $\sum_\gamma \Delta\eta$ distribution is very different from the measured distribution, while the reweighted MC agrees much better with the data. The ratio is consistent with unity except at large $\sum_\gamma \Delta\eta$ where there are few counts and below 2.5 where a $\sim$ 30% excess can be observed in the data

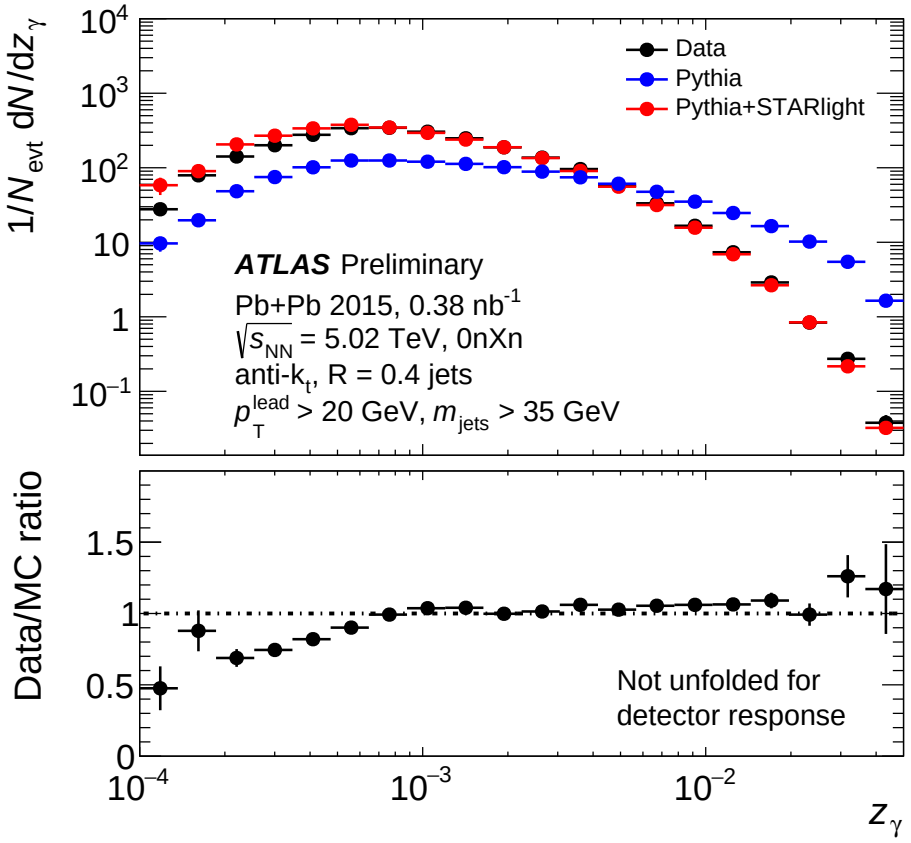

Figure 6: Comparison of data and PYTHIA+STARLIGHT MC z_γ distributions. The top panel shows the z_γ distributions in data (black), PYTHIA (blue), and PYTHIA+STARLIGHT (red). The bottom panel shows the ratio of data to PYTHIA+STARLIGHT. The error bars represent the statistical uncertainties only.

compared to the MC. The shapes of the $\sum_A \Delta\eta$ distribution also agree well between data and MC (not shown) though the fraction of the events with $\sum_A \Delta\eta = 0$ differs between data and reweighted MC.

Figure 8 shows a comparison of the data and MC jet rapidity (left) and mass (right) distributions. As for the previous distributions, the reweighted MC distributions are in much better agreement with the data than the un-reweighted distributions. For both variables, the reweighted MC distributions show a slight excess over the data at more forward rapidities while the data show a small excess over the reweighted MC near the peak of the rapidity distribution.

Figure 9 shows data-MC comparisons for the leading-sub-leading $\Delta\phi$ (left) and jet system H_{T} (right) distributions. Once again, the reweighted MC distributions are in approximate agreement with the data, though a slow variation in the data/MC ratio is observed for the jet mass distribution.

The agreement between the measured distributions shown above and the reweighted MC distributions indicates that PYTHIA is accurately modeling both the direct and resolved contributions of the photo-nuclear collisions. The extent to which the different distributions change under the reweighting indicate the sensitivity of the given observable to the photon spectrum. Since the jet kinematics will also be sensitive to the parton energies, it is likely that the distributions which are most sensitive to the z_γ re-weighting may also be sensitive to nuclear PDF modifications. It should also be noted that the lack of

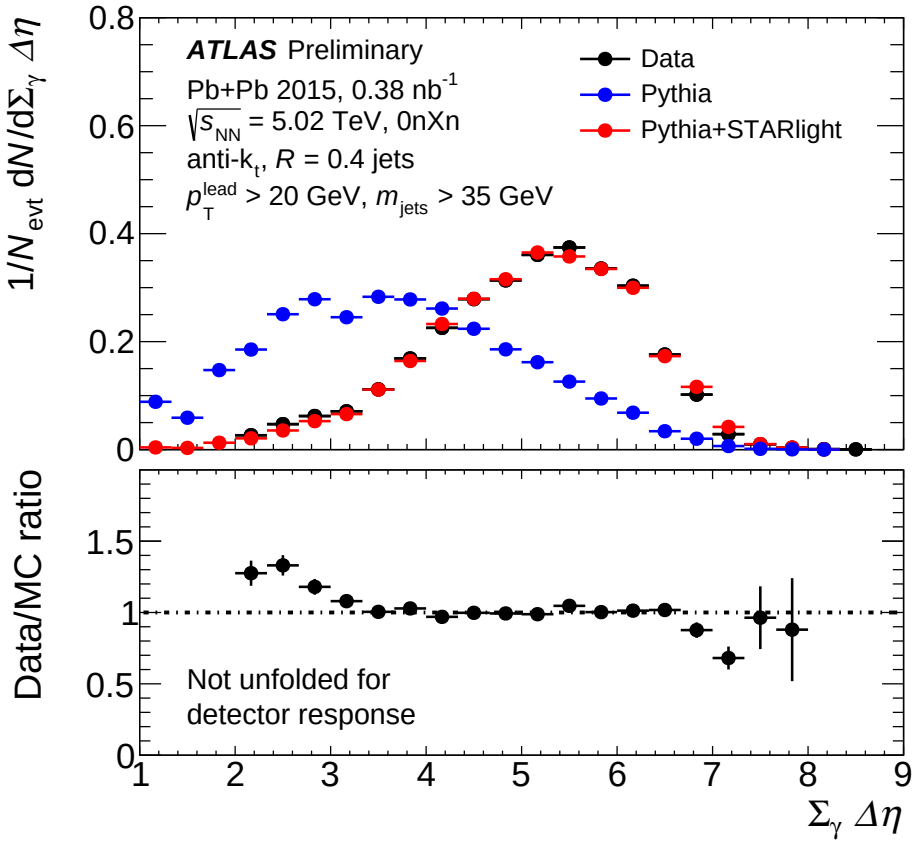

Figure 7: Comparison of data and PYTHIA+STARLIGHT MC $\sum_\gamma \Delta\eta$ distributions. The top panel shows distributions for data (black), PYTHIA (blue), and PYTHIA+STARLIGHT (red). The MC distributions are shown over the full $\sum_\gamma \Delta\eta$ range while the data are required to satisfy the event selection $\sum_\gamma \Delta\eta > 2$. The bottom panel shows the ratio of data to PYTHIA+STARLIGHT. The error bars represent the statistical uncertainties only.

$\gamma + n$ MC simulations and the resulting isospin mismatch with dijet photo-production in Pb+Pb collisions will influence the data-MC agreement even after the STARLIGHT re-weighting is applied.

5.6 Cross-section measurement

The UPC photo-nuclear differential cross-section, uncorrected for jet response is generically calculated using

$$\mathrm{d}\tilde{\sigma} = \frac{1}{\mathcal{L}} \frac{\Delta N}{\varepsilon_{\mathrm{trig}}\, \varepsilon_{\mathrm{sel}}}, \tag{8}$$

where ΔN represents the number of events measured in some bin in the space of kinematic variables used for the cross-section. The tilde on the cross-section provides a reminder that the cross-sections presented here are not unfolded for detector response. In Eq. 8, $\varepsilon_{\mathrm{trig}}$ represents the efficiency of a given trigger, and $\varepsilon_{\mathrm{sel}}$ represents the event selection efficiency. The trigger efficiency depends both on E^{ZDC} and the jet momenta, while $\varepsilon_{\mathrm{sel}}$ is evaluated as a function of z_γ and x_{A}.

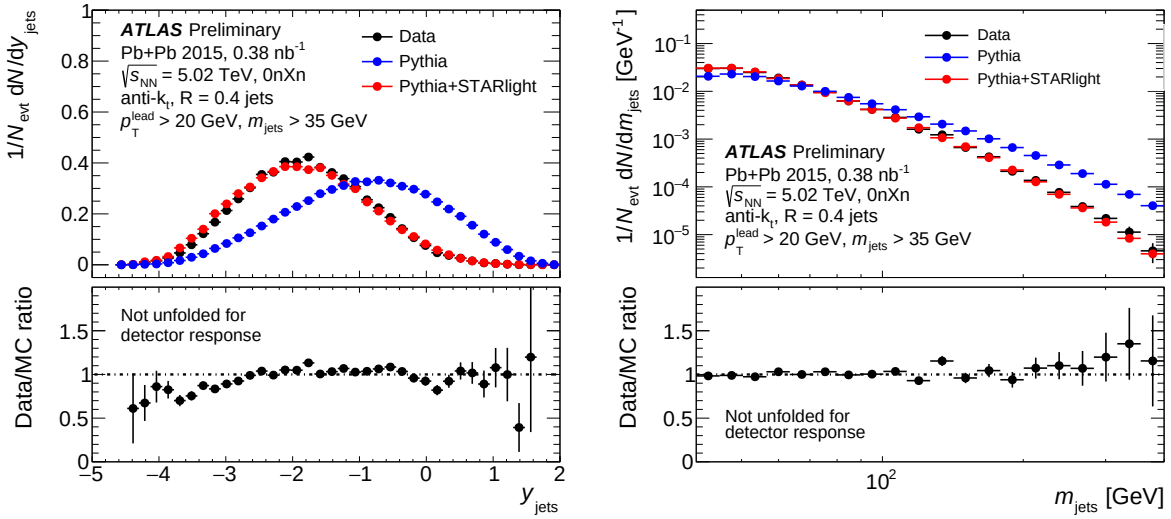

Figure 8: Comparison of data and PYTHIA+STARLIGHT MC jet rapidity distributions for the rapidity (left) and mass (right) of the N-jet system (right). The top panels shows the distributions in data (black), PYTHIA (blue), and PYTHIA+STARLIGHT (red). The bottom panels shows the ratio of data to PYTHIA+STARLIGHT. The error bars represent the statistical uncertainties only.

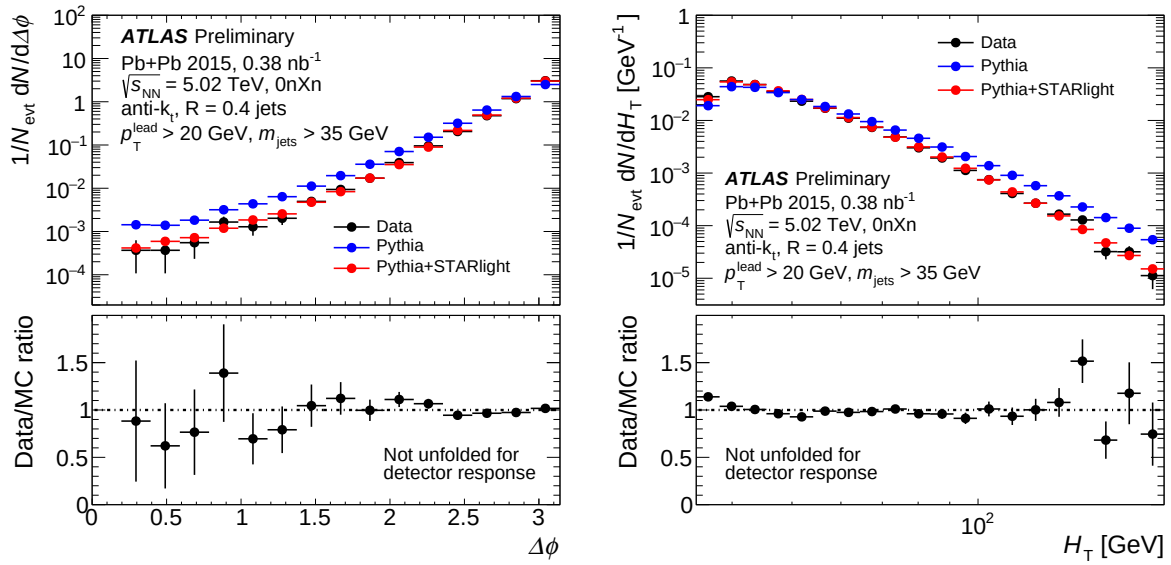

Figure 9: Comparison of data and PYTHIA+STARLIGHT MC leading-sub-leading $\Delta\phi$ (left) and jet H_{T} (right) distributions. The top panels shows the distributions in data (black), PYTHIA (blue), and PYTHIA+STARLIGHT (red). The bottom panels shows the ratio of data to PYTHIA+STARLIGHT. The error bars represent the statistical uncertainties only.

Many of the results in this note are presented in terms of the triple-differential cross-sections, $\mathrm{d}^3\tilde{\sigma}/\mathrm{d}H_\mathrm{T}\,\mathrm{d}x_\mathrm{A}\mathrm{d}z_\gamma$, which is obtained using

$$\frac{\mathrm{d}^3\tilde{\sigma}}{\mathrm{d}H_\mathrm{T}x_\mathrm{A}\mathrm{d}z_\gamma} = \frac{1}{\mathcal{L}}\frac{\Delta N}{\Delta H_\mathrm{T}\,\Delta x_\mathrm{A}\,\Delta z_\gamma}\frac{1}{\varepsilon_\mathrm{trig}\,\varepsilon_\mathrm{sel}}. \tag{9}$$

Here Δx_A, Δz_γ, and ΔH_T represent the sizes of the bins in x_A and z_γ, and H_T, respectively.

The cross-sections are measured within the following fiducial ranges: $35 < m_\mathrm{jets} < 400$ GeV, $-5 < y_\mathrm{jets} < 3$, $35 < H_\mathrm{T} < 200$ GeV, $5\times10^{-4} < x_\mathrm{A} < 1$, and $10^{-4} < z_\gamma < 0.05$. The cross-sections are evaluated using logarithmic binning for m_jets, H_T, z_γ, and x_A.

The event selection efficiency ε_sel differs from unity primarily due to the applied gap requirements. It is evaluated as a function of z_γ and x_A using the MC sample and over most of the fiducial range of the measurement the efficiency is > 99%. However, for $z_\gamma > 0.01$, the $\sum_\gamma \Delta\eta$ selection introduces an inefficiency that is as high as 30% for the smallest x_A values.

The trigger efficiency, $\varepsilon_\mathrm{trig}$, accounts for inefficiency arising from the ZDC component of the UPC trigger, small inefficiencies in the jet trigger described below, and for losses of 0nXn events due to pileup from electromagnetic (EM) dissociation processes. The ZDC trigger inefficiency is ∼ 2% and is approximately independent of the kinematics of the measured photo-nuclear events. The loss of events due to second EM dissociation collisions during the same bunch crossing as a photo-nuclear event and that contribute neutrons in the photon-going direction is estimated using the single EM dissociation cross-section from the RELDIS model [34, 35] which is reported to be 205 ± 10 b [36]. Averaged over the 2015 Pb+Pb run, the EM dissociation induces a 5% inefficiency that is z_γ-,x_A-, and H_T-independent because the EM pileup is uncorrelated with the photo-nuclear collision.

The results from the three primary triggers are combined using exclusive regions in the four-dimensional space (p_Tlead, y_lead, p_Tsublead, y_sublead) as follows:

- The UPC-Jet trigger is used when either $p_\mathrm{Tlead} > 32$ GeV and $|y_\mathrm{lead}| < 3.1$ or $p_\mathrm{Tsublead} > 32$ GeV and $|y_\mathrm{sublead}| < 3.1$.
- The UPC-FWJet trigger is used when the above conditions are not filled and when either $p_\mathrm{Tlead} > 33$ GeVand $|y_\mathrm{lead}| > 3.4$ or $p_\mathrm{Tsublead} > 33$ GeV and $|y_\mathrm{sublead}| > 3.4$.
- The UPC trigger is used when neither of the above conditions is filled.

For each region, the cross-section is evaluated in the space of the above four variables plus the desired kinematic variables and then integrated over (p_Tlead, y_lead, p_Tsublead, y_sublead) to obtain the cross-section in the space of the kinematic variables. The trigger efficiency factor includes corrections of up to 2% and 4% for the UPC-Jet and UPC-FWJet triggers for residual inefficiency in the p_T range where they are used.

Figures 10 and 11 show the cross-sections, $\mathrm{d}^2\tilde{\sigma}/\mathrm{d}x_\mathrm{A}\,\mathrm{d}z_\gamma$ and $\mathrm{d}^2\tilde{\sigma}/\mathrm{d}H_\mathrm{T}\,\mathrm{d}x_\mathrm{A}$, obtained by integrating $\mathrm{d}^3\tilde{\sigma}/\mathrm{d}H_\mathrm{T}\,\mathrm{d}x_\mathrm{A}\mathrm{d}z_\gamma$ over H_T and z_γ, respectively. The coverage in (x_A, z_γ) is constrained by the kinematic range of the measurement. In particular, the minimum m_jets constraint restricts the acceptance of the measurement to the upper right region. This constraint is indicated on the figure by the line which shows the locus of events having $m_\mathrm{jets} = 35$ GeV.

The coverage in the H_T–x_A space is constrained at low H_T by the minimum values for p_Tlead and p_Tsublead used in the analysis. The acceptance is also determined by the range of z_γ values accessible in $\sqrt{s_\mathrm{NN}} = 5.02$ TeV Pb+Pb collisions. The rapidity acceptance of the ATLAS detector also introduces an acceptance restriction at low x_A.

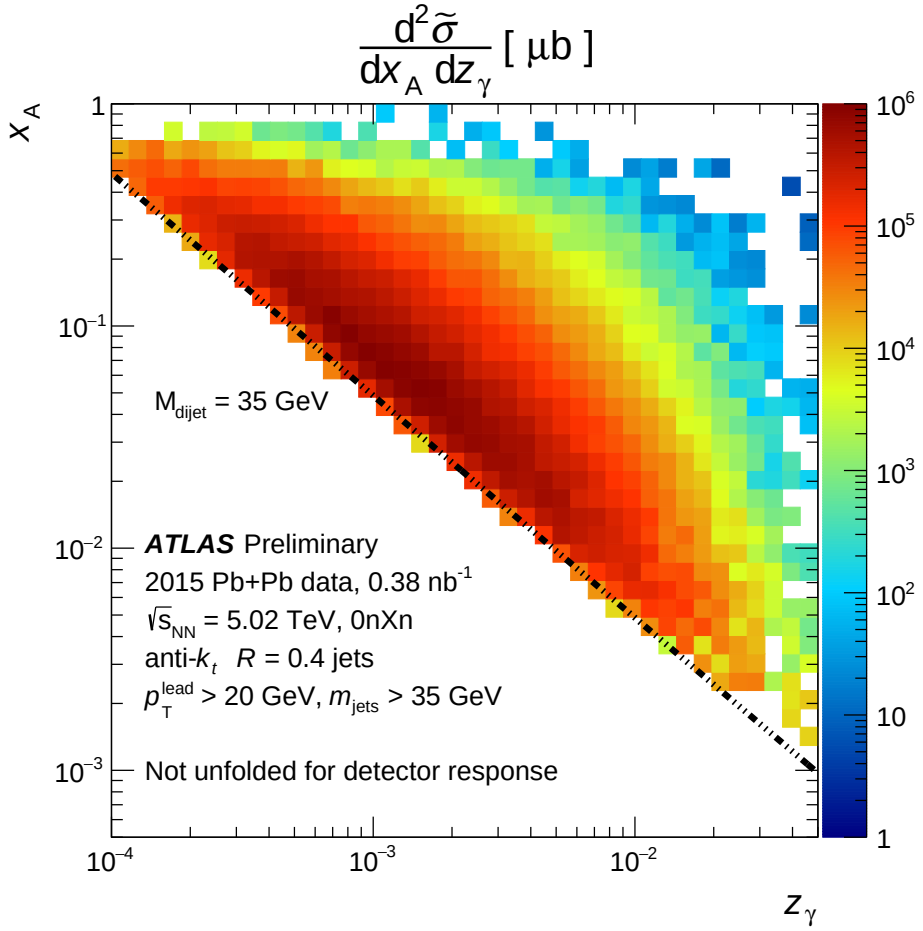

Figure 10: Two-dimensional presentation of the double-differential cross-section, $d^2\tilde{\sigma}/dx_A\, dz_\gamma$, integrated over the H_T range of the measurement, $35 < H_T < 200$ GeV. The dot-dashed line represents the possible (z_γ, x_A) values for jet systems having a mass of 35 GeV– the minimum m_{jets} value for events included in the analysis.

The correlation between the reconstructed z_γ, x_A, and H_T and the corresponding particle- and parton-level quantities was studied in the PYTHIA+STARLIGHT sample. The response in each quantity was found to be approximately symmetric, with events typically reconstructed in the same kinematic bin from which they originated.

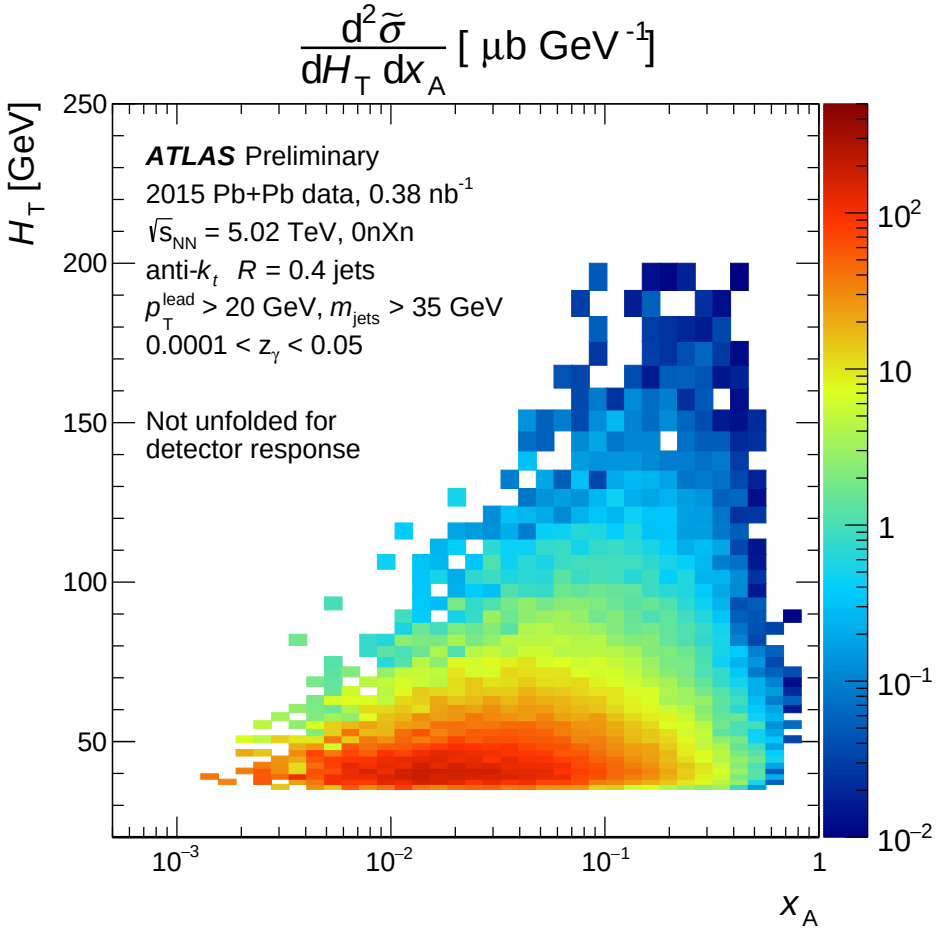

Figure 11: Two-dimensional presentation of the double-differential cross-section, $d^2\tilde{\sigma}/dH_T\,dx_A$, integrated over the full z_γ range used in the analysis.

6 Systematic uncertainties

The primary sources of systematic uncertainty in this measurement are the luminosity measurement, ZDC trigger efficiency and EM dissociation pileup corrections, corrections for event selection efficiency, and uncertainties in the jet response.

As discussed in Sec 3.1, the luminosity calibration for the 2015 Pb+Pb data-taking period has a relative systematic uncertainty of 6.1%. The correction for EM pileup introduces a potential systematic uncertainty due to the uncertainty in the nuclear EM dissociation cross-section. That uncertainty was evaluated to be 0.5%. The systematic uncertainty on the ZDC trigger efficiency correction is conservatively taken to be half the correction, ±1%. All three of these uncertainties are manifestly (luminosity and EM pileup) or approximately (ZDC efficiency) independent of the kinematics of the photo-nuclear scattering and are fully correlated over every bin in measured differential cross-sections. Combined in quadrature they contribute a 6.2% systematic uncertainty on the normalization.

The correction for event selection efficiency introduces potential systematic uncertainties due to imperfect agreement between the data and MC distributions of quantities used in the event selection. The dominant

sources of event selection inefficiency are the requirements on $\sum_\gamma \Delta\eta$ and $\sum_A \Delta\eta$. To estimate the systematic uncertainty on the efficiency correction, each of the gap requirements was separately varied by ± 0.65, the resolution on the gap sum for small $\sum_\gamma \Delta\eta$ and $\sum_A \Delta\eta$ values evaluated using the MC. For each variation, a new efficiency was calculated and applied to the cross-section obtained using the same gap selection. The upward and downward variations were evaluated separately for $\sum_\gamma \Delta\eta$ and $\sum_A \Delta\eta$ and combined in quadrature to obtain an asymmetric systematic uncertainty on the event selection efficiency correction. The estimated systematic is typically a few percent or less except at the largest z_γ values where it varies from $\sim 25\%$ at the extremes of the x_A range to $\sim 10\%$ in the middle of the x_A range.

Systematic uncertainties in the measured cross sections from uncertainties in the jet energy scale and jet energy resolution were evaluated by applying variations to reconstructed jet p_T values in the MC sample and considering the fractional change in the resulting cross section. The procedure was applied to the MC sample instead of the data, so as not to include statistical fluctuations in the latter in the systematics. As the MC distributions, after reweighting, were found to match the measured distributions well, the effect of the systematic variations on the MC sample is expected to be similar to those in the data. The procedure was also applied to the data and the results were found to be compatible modulo features in the data result attributable to statistical fluctuations.

The jet energy resolution (JER) uncertainty was evaluated in the MC sample by adding additional p_T smearing to account for possible under-estimation of the JER in the MC. The evaluation of the JES uncertainties follows from the cross calibration procedure [37]. For each jet in the MC sample, the four-momentum was varied according to 74 nuisance parameters, the majority of which result from statistical and modeling uncertainties in the inter-calibration and *in situ* calibrations.

Separately, contributions to the jet response systematic result from the flavor-dependence of the jet response and the fact that the flavor composition of the photo-nuclear jets is different than that used in the *in situ* calibration. Specifically, the flavor-dependent contribution to the JES systematic uncertainty can be written:

$$\Delta\mathcal{R}_{\text{photo-nuclear}} = \Delta\mathcal{R}_q + \Delta f_g (\mathcal{R}_q - \mathcal{R}_g) + f_g \Delta\mathcal{R}_g \,. \tag{10}$$

Here, $\Delta\mathcal{R}_q$ and $\Delta\mathcal{R}_g$ represent the uncertainties on the quark and gluon JES, respectively, $\mathcal{R}_q - \mathcal{R}_g$ represents the difference in the JES between quarks and gluons, f_g represents the gluon fraction in the photo-nuclear sample, and Δf_g the uncertainty on that fraction. It is assumed that the *in situ* sample is entirely composed of quark jets, and thus $\Delta\mathcal{R}_q$ is removed by the *in situ* correction. The second and third terms are referred to as the *flavor composition* and *flavor response* terms, respectively, and depend on the fraction of gluon jets in photo-nuclear events. The f_g is obtained from studying the gluon fraction in the Pythia photo-nuclear sample including the reweighting. Without additional information, Δf_g was taken to be f_g, i.e. a 100% uncertainty on the gluon flavor fraction was assumed. Both uncertainties are largest at lower p_T and at negative η (opposite the photon-going direction) where the gluon fraction is largest and reach maximal values of 1 and 2% for the response and composition components, respectively.

The jet response systematic uncertainties, combined in quadrature, have a complicated dependence on z_γ and x_A since these have a non-linear dependence on the jet p_T and rapidities. In most cases, the dominant contribution to the jet response systematic uncertainty arises from the *in situ* calibration. However, at small z_γ, x_A, or H_T, the contribution from the JER uncertainty is comparable. Generally, the relative systematic uncertainties on the measured cross-sections rising from jet response are largest for the extreme values of x_A and z_γ where the differential cross-sections are the steepest. At intermediate z_γ and x_A, where the cross-sections are the flattest, the jet response systematic uncertainties are smaller than the

other systematic uncertainties. Also, for large x_A, the jets are typically produced at larger $|\eta|$ where JES systematic uncertainties are larger.

7 Backgrounds

This measurement is potentially sensitive to physical backgrounds from $\gamma + \gamma$ collisions and from hadronic diffraction. These two sources of potential background are discussed in the following sections.

7.1 $\gamma + \gamma \to q\bar{q}$

The same enhancement in the photon flux that allows the measurement of photo-nuclear processes in Pb+Pb collisions also produces a non-negligible rate of $\gamma + \gamma$ processes. Ideally, such scattering processes would leave both nuclei intact, but additional photon exchanges between the nuclei during the scattering can cause one or both to break up and, thus, produce events with the 0nXn topology. The $\gamma + \gamma \to q\bar{q}$ process can produce dijet and multi-jet final states that are similar to those observed in photo-nuclear collisions. However, while the photo-nuclear events are asymmetric in rapidity, the jets produced in $\gamma + \gamma$ processes have a rapidity distribution that is centered at mid-rapidity. As a result, they may contribute in a rapidity region where the photo-nuclear cross-section is small.

The possible background from $\gamma + \gamma \to q\bar{q}$ events has been studied in three different ways. First, di-muon events produced in $\gamma + \gamma \to \mu^+\mu^-$ collisions and measured by ATLAS [10] are used to estimate the rate of $\gamma + \gamma \to q\bar{q}$ events passing the cuts applied in this analysis. Second, the sample of simulated Herwig++ $\gamma + \gamma \to q\bar{q}$ events was analyzed to evaluate the rate for such events passing the analysis selections. Finally, events selected by a jet-based trigger that did not impose the 0nXn requirement was analyzed. Dijet and multi-jet events satisfying the 0n0n topology were studied to provide a data-driven evaluation of the $\gamma + \gamma$ background.

Because the $\gamma + \gamma \to q\bar{q}$ and $\gamma + \gamma \to \mu^+\mu^-$ processes arise from the same QED Feynman diagram, the kinematics of the jets produced in the $q\bar{q}$ process will be similar to those in the $\mu^+\mu^-$ process though the jets will be shifted to lower p_T due to large-angle radiation not contained within the measured jet radius. A comparison of the cross-section measured here with the di-muon cross-section, subject to the constraints, $m_{\mu\mu} > 35$ GeV and $p_T^{\mu} > 17.5$ GeV – the latter to match the H_T requirement imposed in this analysis – shows that at mid-rapidity, the di-muon cross-section is a factor > 100 smaller than the measured photon-nuclear cross-section. However, at more forward rapidity, $y = 2$, the di-muon cross-section is only a factor of ~ 10 smaller. The requirement that events are only accepted when one of the nuclei emits forward neutrons reduces the di-muon cross-section by a factor of ~ 2. More important, however, is that analyzing the events with break-up in the same manner as the photo-nuclear events further substantially reduces the di-muon cross-section.

Consider an event that contains a di-muon pair having a rapidity more than a unit away from mid-rapidity which is analyzed like a photo-nuclear event. If the break-up neutrons are produced in the same direction as the rapidity of the pair, the event will end up at negative rapidity in a region of large photo-nuclear cross-section. However, if the break-up neutrons are produced in the other direction, there will be a large rapidity gap on the nuclear-going side. Those events are efficiently removed by the $\sum_A \Delta\eta < 3$ requirement. Indeed, analyzing the di-muon events in the 0nXn topology as if they were photo-nuclear

events, but allowing for an extra unit of rapidity in the $\sum_A \Delta\eta$ requirement to account for the fragmentation of the jets, yields no events having pair rapidity greater than zero.

An analysis of the Herwig++ $\gamma + \gamma \to q\bar{q}$ events yields a similar result, namely no events having $y_{\text{jets}} > 0$ survive after analyzing the events as if they were photo-nuclear events. Since the ZDC was not included in the simulation, both directions of the nuclear breakup were considered with 50% probability. As with the analysis of the di-muon events, the $\sum_A \Delta\eta < 3$ requirement efficiently removes events that might contribute at forward rapidities. Accounting for the Herwig++ cross-section of $(180 \pm 36)\,\mu\text{b}$ for the generated sample, the cross-section for events passing a photo-nuclear-like cuts at $y_{\text{jets}} < 0$ is comparable to the measured di-muon cross-section. Thus, the observation of no events for $y_{\text{jets}} > 0$ indicates negligible background to the photo-nuclear measurement.

A separate analysis has been performed of events selected by a trigger similar to the UPC-Jet trigger but with no 0nXn condition imposed on the ZDC. To estimate the potential background from $\gamma + \gamma$ events, a 0n0n requirement was imposed – namely that no neutrons were observed in either ZDC. A significant fraction of the events obtained from that sample are clearly photo-nuclear events, as they have a gap on one side, but no significant gap in the other direction. Removing those events by requiring an edge gap of at least one unit on each side and analyzing the remaining events as if they were photo-nuclear events, yielded the same result as above: no events survived with $y_{\text{jets}} > 0$. The resulting constraint on the background is less stringent than the di-muon and Herwig++ constraints, because of the p_{T} threshold of the trigger. Nonetheless, it provides a data-driven confirmation that the $\sum_A \Delta\eta < 3$ requirement is effective at removing these backgrounds.

7.2 Hadronic diffraction

Dijet production in single-diffractive processes [38] can, in principle contribute as background to this measurement. Diffractive processes are usually separated into coherent and incoherent contributions. The coherent contribution involves the entire nucleus and is enhanced relative to pp collisions by a factor of $\sim A^2$. However, it contributes only at very small t values for which hard scattering processes are suppressed. The incoherent component involves diffraction off a single nucleon in the nucleus. Because the nucleons are lightly bound with respect to the energy and momentum transfer scales of the scattering, these processes are sometimes referred to as quasi-diffractive. The incoherent or quasi-diffractive contribution only occurs for impact parameters $b \sim 2R$ since any non-diffractive nucleon-nucleon scattering will destroy the diffractive nature of the Pb+Pb collision. Also, only nucleons at the periphery of the nucleus contribute to incoherent diffraction so the enhancement of the incoherent diffractive cross-section relative to pp collisions is significantly less than a factor of A. Furthermore, quasi-diffractive processes are expected to efficiently break up the nucleus [39, 40] and cause the emission of forward neutrons. Thus, for this measurement which requires the 0nXn topology, the background from diffractive dijet production is expected to be small. A quantitative evaluation of the nuclear breakup probability for quasi-diffractive processes in $\sqrt{s_{\text{NN}}} = 5.02$ TeV collisions would allow a more rigorous statement to be made regarding this potential background.

8 Results

Figures 12-15 show the primary results of this measurement, the differential cross-sections for photo-nuclear production of dijets in events satisfying the 0nXn topology. The results are corrected for trigger and event selection efficiencies but are not unfolded for other detector effects. They are plotted as different sets of one-dimensional slices of $\mathrm{d}^2\tilde{\sigma}/\mathrm{d}H_\mathrm{T}\,\mathrm{d}x_\mathrm{A}$, $\mathrm{d}^2\tilde{\sigma}/\mathrm{d}H_\mathrm{T}\,\mathrm{d}z_\gamma$, and $\mathrm{d}^2\tilde{\sigma}/\mathrm{d}x_\mathrm{A}\,\mathrm{d}z_\gamma$ as a function of one of the other kinematic variables. Specifically, Figure 12 shows the H_T dependence of $\mathrm{d}^2\tilde{\sigma}/\mathrm{d}H_\mathrm{T}\,\mathrm{d}x_\mathrm{A}$ for different bins of x_A; Figure 13 shows the x_A dependence of $\mathrm{d}^2\tilde{\sigma}/\mathrm{d}H_\mathrm{T}\,\mathrm{d}x_\mathrm{A}$ for different intervals of H_T; Figure 14 shows the z_γ dependence of $\mathrm{d}^2\tilde{\sigma}/\mathrm{d}H_\mathrm{T}\,\mathrm{d}z_\gamma$ for different intervals of H_T; Figure 15 shows the x_A dependence of $\mathrm{d}^2\tilde{\sigma}/\mathrm{d}x_\mathrm{A}\,\mathrm{d}z_\gamma$ for different intervals of z_γ. Systematic uncertainties on the cross-sections due to event selection efficiency and jet response are shown on the figures with shaded bands. Not indicated on the figures is an overall systematic uncertainty on the normalization of 6.2% due to luminosity, ZDC trigger efficiency and the EM pileup correction though the last two contributions are negligible compared to the luminosity uncertainty.

The measured cross-sections are compared to the re-weighted PYTHIA+STARLIGHT cross-sections which are represented by the dashed lines. The PYTHIA+STARLIGHT cross-sections are normalized to have the same integral as the data over the measured kinematic range. The agreement between data and Monte-Carlo is good over most of the range of the measurement, though it is less good at the largest and smallest z_γ and x_A values where the cross-sections are particularly sensitive to the kinematic selections in the analysis. The most significant differences between data and MC are observed at low z_γ where even after re-weighting PYTHIA+STARLIGHT exceeds the data by as much as a factor of two (see Figure 6). Aside from this defect, perfect agreement between data and PYTHIA+STARLIGHT should not be expected because of the expected nuclear PDF modifications and because the PYTHIA+STARLIGHT MC sample did not include a sample of photon-neutron events with proper isospin averaging. Nonetheless, the fact that the data and MC agree over a wide range of z_γ and x_A show that the original proposal to study nuclear parton distributions in ultra-peripheral photo-nuclear collisions [9] is realisable, that the resulting cross-sections reflect the expected photon spectrum, and that an event generator is capable of accurately describing the resulting events and the jet kinematics.

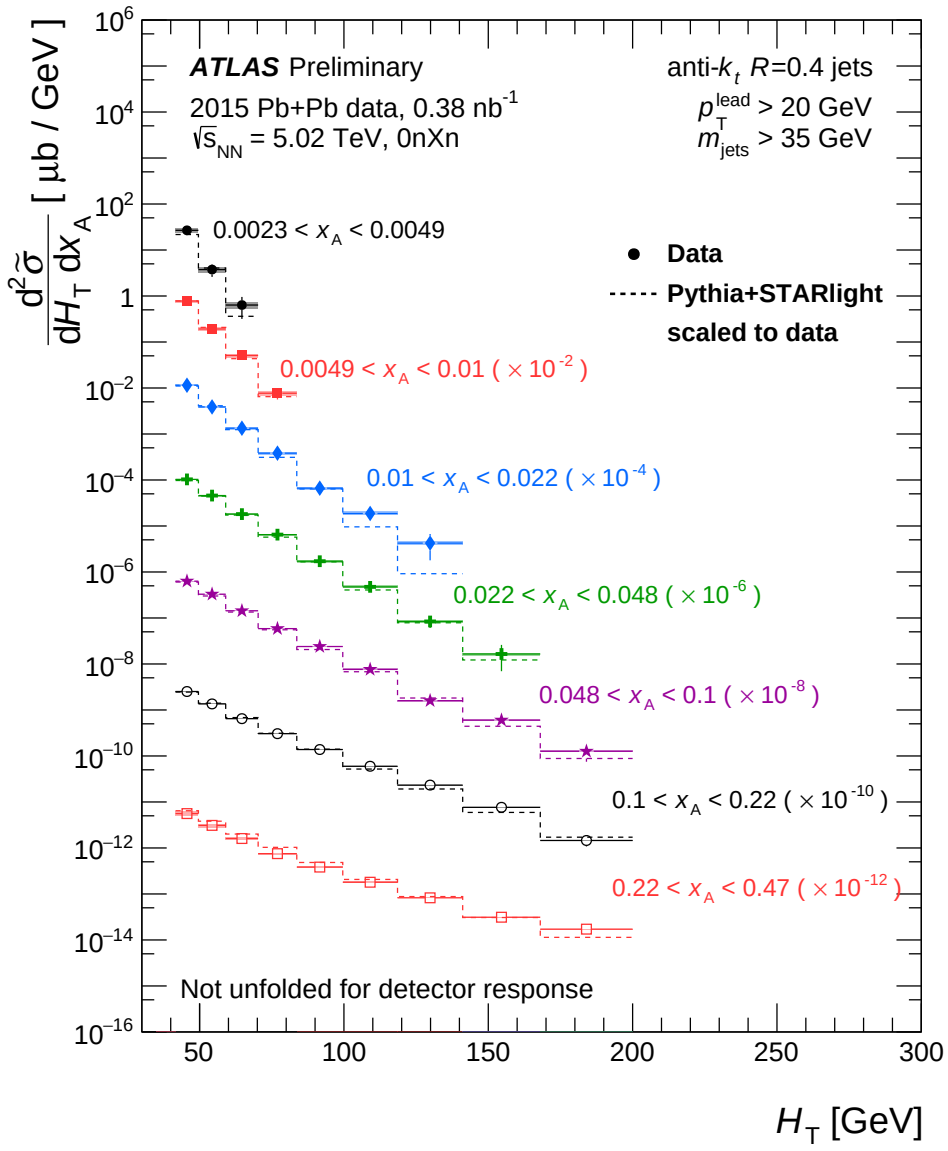

Figure 12: Double-differential cross-section $\mathrm{d}^2\tilde{\sigma}/\mathrm{d}H_\mathrm{T}\,\mathrm{d}x_\mathrm{A}$ as a function of H_T for different bins of x_A. The cross-sections are scaled by successive powers of 100 to improve visibility. The dashed lines represent the cross-section from PYTHIA+STARLIGHT scaled to have the same integral as the data within the fiducial region of the measurement.

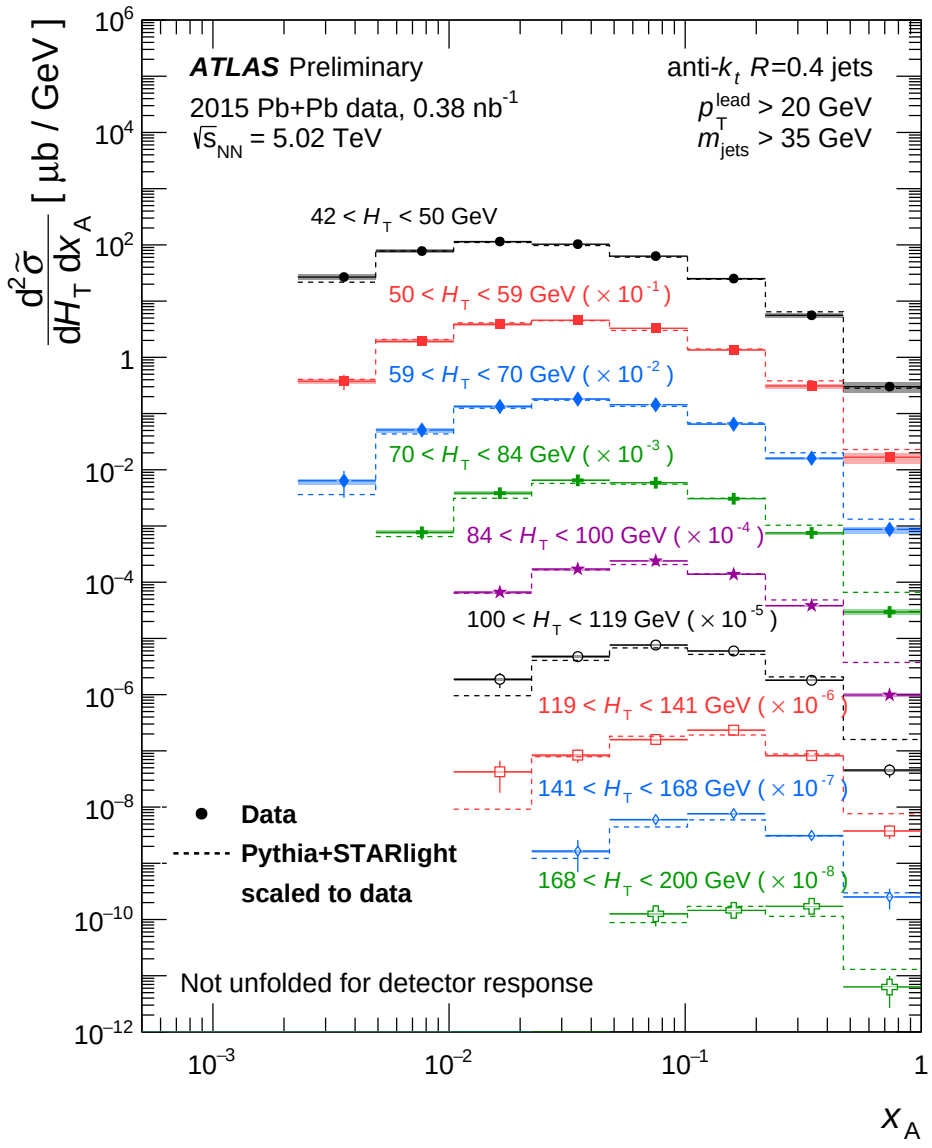

Figure 13: Double-differential cross-section $\mathrm{d}^2\tilde{\sigma}/\mathrm{d}H_\mathrm{T}\,\mathrm{d}x_\mathrm{A}$ as a function of x_A for different bins of H_T. The cross-sections are scaled by successive powers of 10 to improve visibility. The dashed lines represent the cross-section from PYTHIA+STARLIGHT scaled to have the same integral as the data within the fiducial region of the measurement.

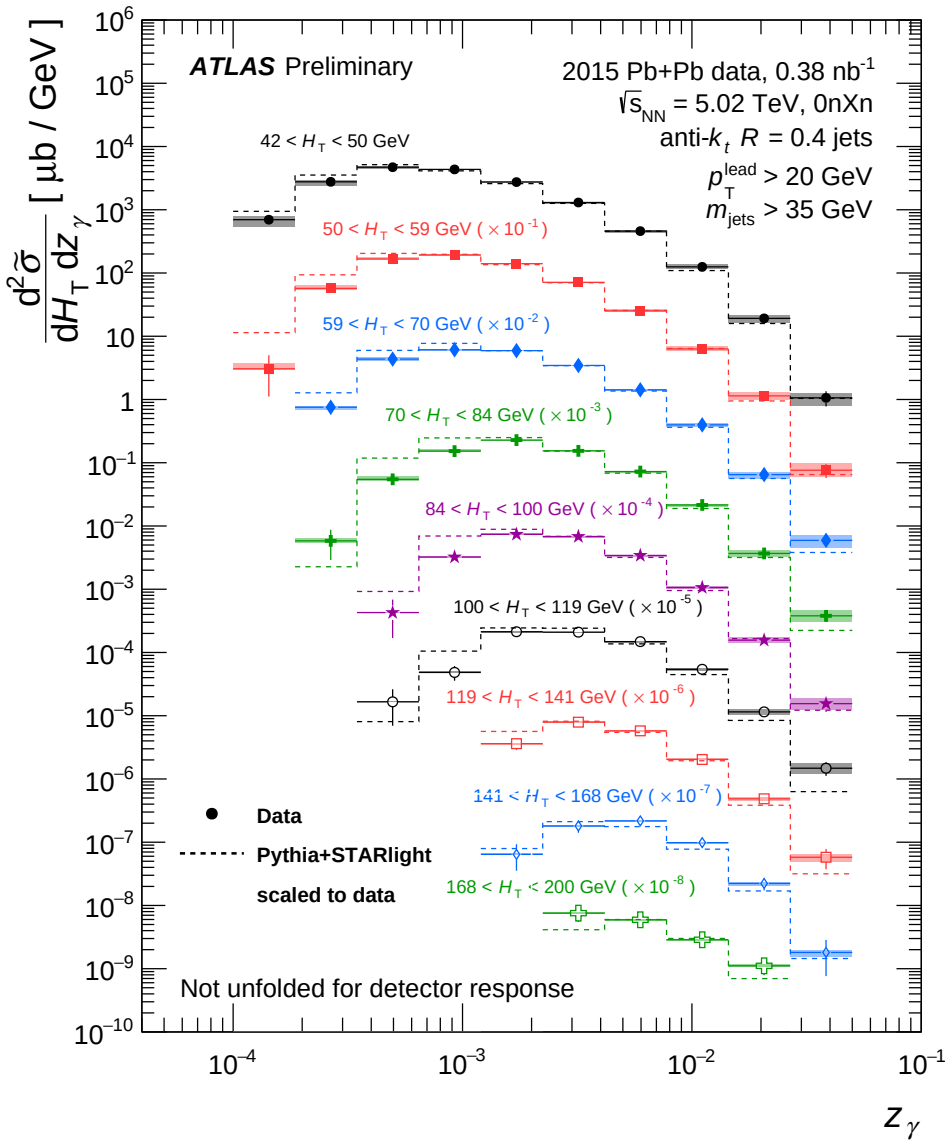

Figure 14: Double-differential cross-section $\mathrm{d}^2\tilde{\sigma}/\mathrm{d}H_\mathrm{T}\,\mathrm{d}z_\gamma$ as a function of z_γ for different bins of H_T. The cross-sections are scaled by successive powers of 10 to improve visibility. The dashed lines represent the cross-section from PYTHIA+STARLIGHT scaled to have the same integral as the data within the fiducial region of the measurement.

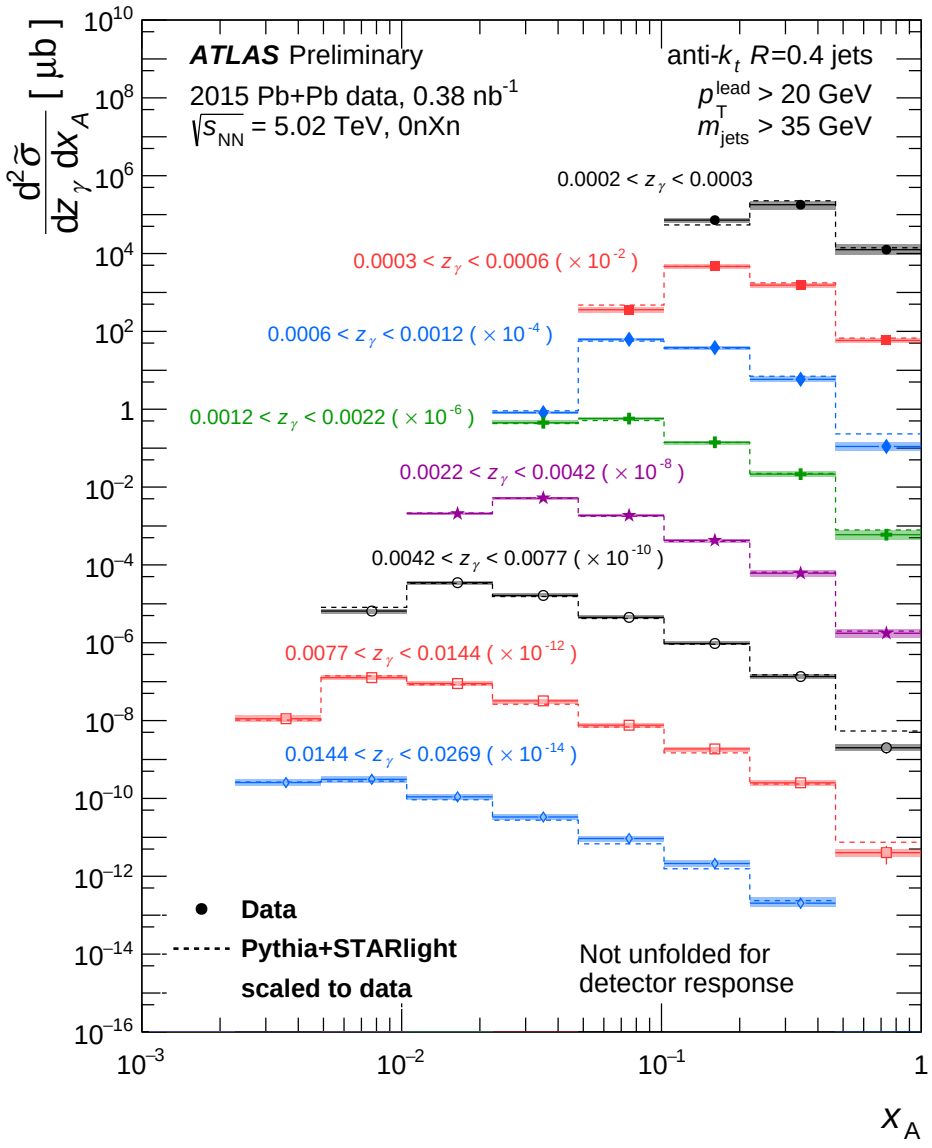

Figure 15: Double-differential cross-section $\mathrm{d}^2\tilde{\sigma}/\mathrm{d}x_\mathrm{A}\,\mathrm{d}z_\gamma$ as a function of x_A for different bins of z_γ. The cross-sections are scaled by successive powers of 100 to improve visibility. The dashed lines represent the cross-section from PYTHIA+STARLIGHT scaled to have the same integral as the data within the fiducial region of the measurement.

9 Conclusion

ATLAS has performed a measurement of photo-nuclear di/multi-jet production in ultra-peripheral Pb+Pb collisions at a nucleon center of mass energy $\sqrt{s_{\rm NN}} = 5.02$ TeV using a total Pb+Pb integrated luminosity of 380 μb^{-1}. This measurement includes both direct and resolved photon events satisfying the 0nXn topology and $\sum_{\gamma} \Delta\eta > 2$ and $\sum_{A} \Delta\eta < 3$ gap requirements. Jets are reconstructed using the anti-k_t algorithm with $R = 0.4$ for $p_{\rm T}^{\rm jet} > 15$ GeV and $|\eta_{\rm jet}| < 4.4$. Events used in the measurement are required to have $20 < p_{\rm T lead} < 100$ GeV and $35 < m_{\rm jets} < 400$ GeV. Results are presented for differential cross-sections as a function of z_γ $x_{\rm A}$, and $H_{\rm T}$, in intervals of the other variables over the fiducial ranges $10^{-3} < x_{\rm A} < 1$ and $10^{-4} < z_\gamma < 0.05$, and $35 < H_{\rm T} < 200$ GeV. The measured cross-sections are corrected for trigger and event selection efficiencies but are not unfolded for other detector effects. The results are compared to Pythia $\gamma + p$ simulations re-weighted to match the photon spectrum obtained from STARLight. The Pythia+STARLight MC provides a good description of the data over a wide range of z_γ, $x_{\rm A}$, and $H_{\rm T}$, values.

These results represent substantial progress towards the experimental realization of the original proposal to study nuclear PDFs in ultra-peripheral collisions using photo-nuclear dijet production [9]. The next step will be to provide measurements that are unfolded for detector response and that can be compared directly to theoretical calculations. The extraction of the PDFs will necessarily depend on the application of NLO calculations of photo-production (e.g. [41, 42, 43]) to the conditions of this measurement. The precision of the extracted PDFs will also depend on control of the resolved photon contribution.

References

[1] K. J. Eskola, V. J. Kolhinen, and C. A. Salgado, *The scale dependent nuclear effects in parton distributions for practical applications*, Eur. Phys. J. **C9** (1999) 61–68, arXiv:hep-ph/9807297 [hep-ph].

[2] L. L. Frankfurt and M. I. Strikman, *Shadowing and Enhancement of Quark Distributions in Nuclei at Small X*, Nucl. Phys. **B316** (1989) 340–354.

[3] N. Armesto, *Nuclear shadowing*, J. Phys. **G32** (2006) R367–R394, arXiv:hep-ph/0604108 [hep-ph].

[4] A. H. Mueller and J. Qiu, *Gluon Recombination and Shadowing at Small Values of x*, Nucl. Phys. **B268** (1986) 427–452.

[5] I. Balitsky, *Operator expansion for high-energy scattering*, Nucl. Phys. **B463** (1996) 99–160, arXiv:hep-ph/9509348 [hep-ph].

[6] Y. V. Kovchegov, *Small x F(2) structure function of a nucleus including multiple pomeron exchanges*, Phys. Rev. **D60** (1999) 034008, arXiv:hep-ph/9901281 [hep-ph].

[7] K. J. Eskola, H. Paukkunen, and C. A. Salgado, *EPS09: A New Generation of NLO and LO Nuclear Parton Distribution Functions*, JHEP **04** (2009) 065, arXiv:0902.4154 [hep-ph].

[8] K. Kovarik et al., *nCTEQ15 - Global analysis of nuclear parton distributions with uncertainties in the CTEQ framework*, Phys. Rev. **D93** (2016) 085037, arXiv:1509.00792 [hep-ph].

[9] M. Strikman, R. Vogt, and S. N. White, *Probing small x parton densities in ultraperipheral AA and pA collisions at the LHC*, Phys. Rev. Lett. **96** (2006) 082001, arXiv:hep-ph/0508296 [hep-ph].

[10] ATLAS Collaboration, *Measurement of high-mass dimuon pairs from ultraperipheral lead-lead collisions at* $\sqrt{s_{\rm NN}} = 5.02$ *TeV with the ATLAS detector at the LHC*, ATLAS-CONF-2016-025. https://cds.cern.ch/record/2157689.

[11] STAR Collaboration, C. Adler et al., *Coherent* ρ^0 *production in ultraperipheral heavy ion collisions*, Phys. Rev. Lett. **89** (2002) 272302, arXiv:nucl-ex/0206004 [nucl-ex].

[12] STAR Collaboration, B. I. Abelev et al., ρ^0 *photoproduction in ultraperipheral relativistic heavy ion collisions at* $\sqrt{s_{NN}} = 200$ *GeV*, Phys. Rev. **C77** (2008) 034910, arXiv:0712.3320 [nucl-ex].

[13] ALICE Collaboration, E. Abbas et al., *Charmonium and* e^+e^- *pair photoproduction at mid-rapidity in ultra-peripheral Pb-Pb collisions at* $\sqrt{s_{\rm NN}} = 2.76$ *TeV*, Eur. Phys. J. **C73** (2013) 2617, arXiv:1305.1467 [nucl-ex].

[14] ALICE Collaboration, B. Abelev et al., *Coherent* J/ψ *photoproduction in ultra-peripheral Pb-Pb collisions at* $\sqrt{s_{NN}} = 2.76$ *TeV*, Phys. Lett. **B718** (2013) 1273–1283, arXiv:1209.3715 [nucl-ex].

[15] ZEUS Collaboration, S. Chekanov et al., *Dijet photoproduction at HERA and the structure of the photon*, Eur. Phys. J. **C23** (2002) 615–631, arXiv:hep-ex/0112029 [hep-ex].

[16] H1 Collaboration, C. Adloff et al., *Measurement of dijet cross-sections in photoproduction at HERA*, Eur. Phys. J. **C25** (2002) 13–23, arXiv:hep-ex/0201006 [hep-ex].

[17] ZEUS Collaboration, M. Derrick et al., *Study of the photon remnant in resolved photoproduction at HERA*, Phys. Lett. **B354** (1995) 163–177, arXiv:hep-ex/9505001 [hep-ex].

[18] ATLAS Collaboration, *The ATLAS Experiment at the CERN Large Hadron Collider*, JINST **3** (2008) S08003.

[19] ATLAS collaboration, *Improved luminosity determination in pp collisions at* $\sqrt{s} = 7$ *TeV using the ATLAS detector at the LHC*, Eur. Phys. J. **C73** (2013) 2518, arXiv:1302.4393 [hep-ex].

[20] T. Sjostrand, S. Mrenna, and P. Z. Skands, *PYTHIA 6.4 Physics and Manual*, JHEP **0605** (2006) 026, arXiv:hep-ph/0603175.

[21] P. Z. Skands, *Tuning Monte Carlo Generators: The Perugia Tunes*, Phys. Rev. **D82** (2010) 074018, arXiv:1005.3457 [hep-ph].

[22] G. A. Schuler and T. Sjostrand, *Low and high mass components of the photon distribution functions*, Z. Phys. **C68** (1995) 607–624, arXiv:hep-ph/9503384 [hep-ph].

[23] G. A. Schuler and T. Sjostrand, *Parton distributions of the virtual photon*, Phys. Lett. **B376** (1996) 193–200, arXiv:hep-ph/9601282 [hep-ph].

[24] M. Bahr et al., *Herwig++ Physics and Manual*, Eur. Phys. J. **C58** (2008) 639–707, arXiv:0803.0883 [hep-ph].

[25] S. R. Klein, J. Nystrand, J. Seger, Y. Gorbunov, and J. Butterworth, *STARlight: A Monte Carlo simulation program for ultra-peripheral collisions of relativistic ions*, Comput. Phys. Commun. **212** (2017) 258–268, arXiv:1607.03838 [hep-ph].

[26] GEANT4 Collaboration, S. Agostinelli et al., *GEANT4: A simulation toolkit*, Nucl. Instrum. Meth. **A 506** (2003) 250–303.

[27] ATLAS Collaboration, *The ATLAS Simulation Infrastructure*, Eur. Phys. J. **C70** (2010) 823–874.

[28] ATLAS Collaboration, *Charged-particle distributions at low transverse momentum in $\sqrt{s}$ = 13 TeV pp interactions measured with the ATLAS detector at the LHC*, Eur. Phys. J. **C76** (2016) 502, arXiv:1606.01133 [hep-ex].

[29] ATLAS Collaboration, *Topological cell clustering in the ATLAS calorimeters and its performance in LHC Run 1*, submitted to EPJC (2016), arXiv:1603.02934 [hep-ex].

[30] M. Cacciari, G. P. Salam, and G. Soyez, *The anti-k_t jet clustering algorithm*, JHEP **04** (2008) 063, arXiv:0802.1189.

[31] ATLAS Collaboration, *Measurement of the jet radius and transverse momentum dependence of inclusive jet suppression in lead–lead collisions at $\sqrt{s_{\rm NN}}$ = 2.76 TeV with the ATLAS detector*, Phys. Lett. B **719** (2013) 220, arXiv:1208.1967 [hep-ex].

[32] ATLAS Collaboration, *Jet energy measurement and its systematic uncertainty in proton-proton collisions at $\sqrt{s}$ = 7 TeV with the ATLAS detector*, Eur. Phys. J. **C75** (2015) 17, arXiv:1406.0076 [hep-ex].

[33] ATLAS Collaboration, *Rapidity gap cross sections measured with the ATLAS detector in pp collisions at $\sqrt{s}$ = 7 TeV*, Eur. Phys. J. **C72** (2012) 1926, arXiv:1201.2808 [hep-ex].

[34] I. A. Pshenichnov, I. N. Mishustin, J. P. Bondorf, A. S. Botvina, and A. S. Ilinov, *Nuclear multifragmentation induced by electromagnetic fields of ultrarelativistic heavy ions*, Phys. Rev. **C57** (1998) 1920–1926, arXiv:nucl-th/9711030 [nucl-th].

[35] I. A. Pshenichnov, *Electromagnetic excitation and fragmentation of ultrarelativistic nuclei*, Phys. Part. Nucl. **42** (2011) 215–250.

[36] I. Pshenichnov and U. Dmitrieva, *On forward protons and photons produced in PbPb collisions at the LHC*, in *Workshop on Proton and Photon-induced nuclear collisions at the LHC*. 2016. https://indico.cern.ch/event/487649/contributions/2212732/attachments/1306023/1951906/Pshenichnov_CERN_July_2016.pdf.

[37] *Jet energy scale and its uncertainty for jets reconstructed using the ATLAS heavy ion jet algorithm*, ATLAS Collaboration, ATLAS-CONF-2015-016. https://cds.cern.ch/record/2008677.

[38] ATLAS Collaboration, *Dijet production in $\sqrt{s}$ = 7 TeV pp collisions with large rapidity gaps at the ATLAS experiment*, Phys. Lett. **B754** (2016) 214–234, arXiv:1511.00502 [hep-ex].

[39] L. Frankfurt, V. Guzey, and M. Strikman, *Leading twist coherent diffraction on nuclei in deep inelastic scattering at small x and nuclear shadowing*, Phys. Lett. **B586** (2004) 41–52, arXiv:hep-ph/0308189 [hep-ph].

[40] A. Accardi et al., *Electron Ion Collider: The Next QCD Frontier*, Eur. Phys. J. **A52** (2016) 268, arXiv:1212.1701 [nucl-ex].

[41] M. Klasen and G. Kramer, *Inclusive two jet production at HERA: Direct and resolved cross-sections in next-to-leading order QCD*, Z. Phys. **C76** (1997) 67–74, arXiv:hep-ph/9611450 [hep-ph].

[42] S. Frixione and G. Ridolfi, *Jet photoproduction at HERA*, Nucl. Phys. **B507** (1997) 315–333, arXiv:hep-ph/9707345 [hep-ph].

[43] P. Aurenche, L. Bourhis, M. Fontannaz, and J. P. Guillet, *NLO Monte Carlo approach in one jet or two jets photoproduction*, Eur. Phys. J. **C17** (2000) 413–421, arXiv:hep-ph/0006011 [hep-ph].